All-Electrochemical Nanofabrication of Stacked Ternary Metal Sulfide/Graphene Electrodes for High-Performance Alkaline Batteries

(article starts on next page)

All-Electrochemical Nanofabrication of Stacked Ternary Metal Sulfide/Graphene Electrodes for High-Performance Alkaline Batteries

Jaime S. Sanchez, Zhenyuan Xia,* Nagaraj Patil, Rebecca Grieco, Jinhua Sun, Uta Klement, Ren Qiu, Meganne Christian, Fabiola Liscio, Vittorio Morandi, Rebeca Marcilla,* and Vincenzo Palermo*

Energy-storage materials can be assembled directly on the electrodes of a battery using electrochemical methods, this allowing sequential deposition, high structural control, and low cost. Here, a two-step approach combining electrophoretic deposition (EPD) and cathodic electrodeposition (CED) is demonstrated to fabricate multilayer hierarchical electrodes of reduced graphene oxide (rGO) and mixed transition metal sulfides (NiCoMnS$_x$). The process is performed directly on conductive electrodes applying a small electric bias to electro-deposit rGO and NiCoMnS$_x$ in alternated cycles, yielding an ideal porous network and a continuous path for transport of ions and electrons. A fully rechargeable alkaline battery (RAB) assembled with such electrodes gives maximum energy density of 97.2 Wh kg^{-1} and maximum power density of 3.1 kW kg^{-1}, calculated on the total mass of active materials, and outstanding cycling stability (retention 72% after 7000 charge/discharge cycles at 10 A g^{-1}). When the total electrode mass of the cell is considered, the authors achieve an unprecedented gravimetric energy density of 68.5 Wh kg^{-1}, sevenfold higher than that of typical commercial supercapacitors, higher than that of Ni/Cd or lead–acid Batteries and similar to Ni–MH Batteries. The approach can be used to assemble multilayer composite structures on arbitrary electrode shapes.

1. Introduction

Nanoengineering-based approaches have demonstrated numerous benefits for improved electrochemical performances when it comes to the design and fabrication of electrode materials for energy storage.[1–5] The synthesis of electrode materials with an optimal nano-structure is crucial to enhance active surface area for high active-material utilization (thus, high capacities) and to shorten diffusion lengths for fast ion/electron transfer; however the random dense packing and agglomeration in conventional electrodes lead to low tap density and capacity fading during cycling.[6] Therefore, a selective, versatile and systematic approach, tuning material design and composition to produce large-scale and long-life electrodes for different battery technologies remains an enormous challenge.[7,8]

In order to fill the gap between commercial lithium-ion batteries (LIBs) which present unresolved safety issues (fire

J. S. Sanchez, Z. Xia, J. Sun, U. Klement, V. Palermo
Industrial and Materials Science
Chalmers University of Technology
Göteborg 41258, Sweden
E-mail: zhenyuan@chalmers.se

J. S. Sanchez, N. Patil, R. Grieco, R. Marcilla
Electrochemical Processes Unit
IMDEA Energy Institute
Móstoles 28935, Spain
E-mail: rebeca.marcilla@imdea.org

Z. Xia, V. Palermo
Consiglio Nazionale delle Ricerche
Istituto per la Sintesi Organica e la Fotoreattività
Bologna 40129, Italy
E-mail: palermo@isof.cnr.it

R. Qiu
Department of Physics
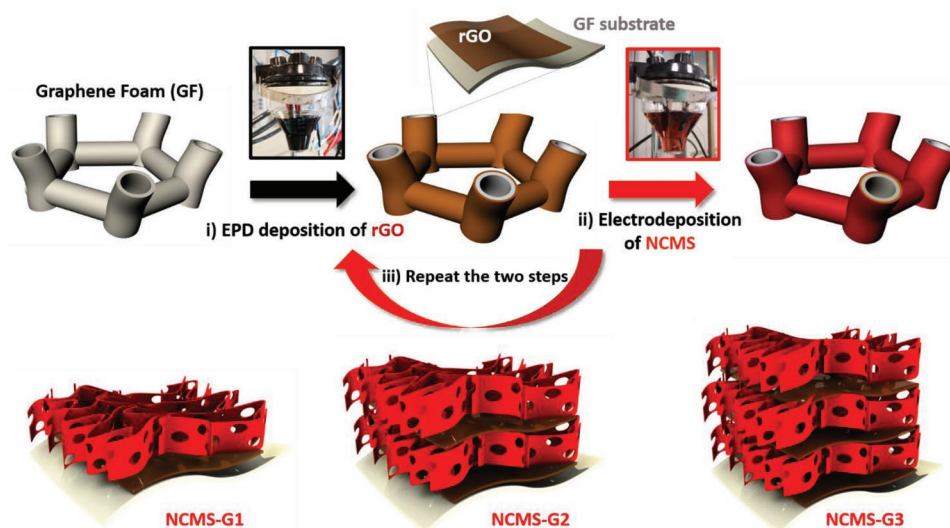Chalmers University of Technology
Göteborg 41258, Sweden

M. Christian, F. Liscio, V. Morandi
Consiglio Nazionale delle Ricerche
Istituto per la Microelettronica e i Microsistemi
Bologna 40129, Italy

ADVANCED
SCIENCE NEWS
www.advancedsciencenews.com

NANO · MICRO
small
www.small-journal.com

Scheme 1. Schematic illustration of the preparation process for multilayer rGO/MTMS graphitic foam architectures.

and/or explosion hazard) and the promising but still under-developed safer solid-state batteries, rechargeable alkaline batteries (RABs) with aqueous electrolyte are considered as alternative choices with relatively high energy density, large power density, and exceptional safety.[9] In contrast to the reversible intercalation/de-intercalation chemistry of aqueous alkali-ion and metal-ion batteries, RABs are mainly based on faradaic processes that involve single- or multi-electron reactions.[10] Transition metal compounds (oxides/hydroxides and sulfides) with versatile morphologies have been vastly investigated for RABs and supercapacitors (SCs) due to their mineral abundance, low-cost, and high capacities reported.[11–16] Among them, mixed transition metal sulfides (MTMSs) have spurred unprecedented interest due to their rich redox states and high electrical/electrochemical performance compared to oxide/hydroxide analogs.[17,18] These MTMSs exhibit relatively high electrical conductivity owing to the electron transfer between cations with different valences, which greatly affects the strength of the surface-intermediate bonds and depends on the chemical structure of the surface.[17] However, the use of MTMSs for practical electronic and electrochemical applications is still hindered by their significant volume change during charge/discharge, which negatively affects the overall cycling stability in final devices.[19,20]

Graphene is a monoatomic sp^2-bonded carbon layer with fascinating physico-chemical properties such as high surface area, excellent electrical conductivity, and good mechanical strength.[21] Therefore, MTMSs can be hybridized with graphene in different ways to enhance the electrochemical/electrocatalytic performance of the pure components due to possible synergistic effects.[19,22–24] For instance, carbonaceous materials such as graphene can effectively enhance the electrical properties and limit the volume expansion of sulfides, extending the longevity of the electrode.[25] However, these materials are commonly synthesized as mixtures or slurries with a random, uncontrolled structure. Their fabrication often requires the addition of significant amounts of binders, conductive agents, high-temperature treatments, time-consuming and multistep processes; this is undesirable for industrial

applications. A smart way to circumvent these limitations is the use of electrochemical methods which allow a tailor-made design of the structure of the hybrid electrode while avoiding the use of additives or binders. Given that the coating is always performed on conductive electrodes, it is very simple to apply a small electric bias to electro-deposit the active materials, in this case, MTMSs, directly on the desired substrate. In previous works, we used electrochemical techniques with success to coat graphene-based materials with metal oxides on structural substrates, that is, carbon fibers,[26] or complex 3D foams.[27] Moreover, these methods allowed us not only to obtain uniform coatings with controlled composition and film thickness but also to invent a robust modular approach to produce multi-layered composites of graphene and metal oxides to be used as electrodes for batteries.[28] The electrostatic layer-by-layer self-assembly technique provides an effective approach for the fabrication of a variety of ordered multilayer film materials with controllable architecture and properties.[29–31] The multilayer approach allows to control the number of layers, their composition, thickness, and physico-chemical properties varying the type of charged species deposited and the number of cycles accordingly, to finally obtain the ideal, predesigned architecture.[32]

Here, we present a new approach based on a combination of two methods, both comprising an electric bias applied to the target electrode, but exploiting different mechanisms:

1) In cathodic electrodeposition (CED), the electric bias triggers the synthesis of the material directly on the surface of the electrode, by decomposition of soluble precursors.
2) In electrophoretic deposition (EPD), the electric bias acts on pre-existing charged particles, attracting them via long-ranged electric field, generating a Coulomb force.

The combination of such methods allows the production of a novel multilayer system consisting of reduced graphene oxide (rGO) layers and hierarchical $NiCoMnS_x$ (NCMS) nanosheet arrays (**Scheme 1**). These multilayers are deposited on an ideal electrode substrate, that is, a 3D graphene foam (GF).

**ADVANCED
SCIENCE NEWS**
www.advancedsciencenews.com

**NANO · MICRO
small**
www.small-journal.com

This kind of 3D graphene structures can be ideal electrodes for batteries, featuring high electrical conductivity (≈ 1000 S m^{-1}), high porosity ($\approx 99.7\%$), low density (≈ 0.6 mg cm^{-2}), large specific surface area (≈ 850 m^2 g^{-1}), and effective multidimensional electrolyte-accessible channels.[33] First, we coated a thin layer of rGO on GF using EPD, to further enhance the adhesion and stability of the active material. Then, we used CED to deposit the NCMS on rGO, forming an array of redox-active interconnected NCMS nanosheets. The modular coating process could be repeated several times, electrochemically coating selectively rGO layers and NiCoMnS$_x$ nanosheets to obtain a hierarchical multilayer structure. In such a structure, the rGO sheets act both as nano-pillars to separate the sulfide nanosheets, which buffer the volume changes of the undergone sulfides, and as electrical connections to the sulfides, thereby creating a high mass loading of NCMS while keeping the series resistance low.

The combination of different electrochemical techniques (electrophoretic and cathodic) allowed us to fabricate high electrochemical performance cathodes for RABs. Tuning EPD and CED conditions and number of layers, we could significantly boost the electrochemical performance of NCMS nanosheets in alkaline aqueous electrolyte. Sandwich-like layered composite materials possess a high contact area and can expose many active sites, which exhibit great potential in energy storage applications. They provide ideal conditions for facile penetration of the electrolyte and accommodation of the strain induced by the volume change during electrochemical reactions, thus bringing higher efficiency for the electrochemical device.[34] Furthermore, we assembled a novel full RAB with the multilayer rGO/MTMSs as cathode and an anthraquinone-based conjugated microporous polymer (IEP-11) as anode, outperforming state-of-the-art alkaline batteries, operating up to 1.6 V and demonstrating a stable cyclability of 72% over 7000 cycles at 10 A g^{-1}.

2. Results and Discussion

### 2.1. Structural and Morphological Investigations

A schematic representation of the multilayer formation along with the systematic approach used for the combination of electrochemical methods is illustrated in Scheme 1, as follows: i) EPD coating of rGO from DMF onto the GF; ii) CED via cyclic voltammetry (CV) of NCMS from water/EtOH co-solvent solution; iii) repetition of previous steps to create multilayer 3D structures. Details of the deposition chemistry used are in the Experimental Section (Section 4).

The surface morphology and nanostructures of the different samples synthesized were analyzed using scanning electron microscopes (SEM) equipped with a field emission gun. We first produced a continuous 3D GF using CVD on a sacrificial nickel template. After removing the nickel in acid, we obtained an all-graphene free-standing substrate, replicating the shape of the interconnected 3D structure of the nickel template (Figure S1, Supporting Information). Initial attempts of direct growth of MTMSs on GF surface failed, resulting in poor adhesion of the NiCoMnS$_x$ material, with detached flakes or cracks (**Figure** 1a).

In order to avoid the formation of cracks and detachment of NiCoMnS$_x$ flakes from the GF surface, we used a first layer coating of rGO acting as a primer. RGO has good affinity with graphene thanks to its extensive, graphene-like sp^2 areas, but maintains a high number of polar groups which can act as adhesion points for polar materials. The rGO coating improved the deposition, yielding a uniform coating of NiCoMnS$_x$ with no microscopic delamination and cracks (Figure 1b,c). We could produce different multi-layer structures by simple repetition of the two coating steps (see Figure S2, Supporting Information). Hereafter, we name NCMS-G1, G2, G3, etc. multilayer samples obtained after 1,2,3 cycles. Instead, repeated deposition of sulfides without rGO deposition did not yield coherent samples, suggesting that the rGO coating layer helps decorate sulfide nanosheets due to the oxygen functional groups on its surface, and also acts as a binder and a conductive spacer, favoring further NiCoMnS$_x$ deposition. For comparison, an NCMS-G1* sample was also produced with no spacers, that is, with only one initial coating step of rGO followed by 10 cycles of electrodeposition of sulfides. Cracking and agglomeration on the nano-wall array were observed (Figure S3, Supporting Information). The maximum loading achievable per CED was limited to 5 CV cycles (≈ 0.4 mg cm^{-2} per CV cycle).[27,28]

SEM imaging (Inset Figure 1b) shows that the sulfide coating is formed by nanosheet arrays uniformly interconnected and distributed on the graphene surface with an average pore size of 50–100 nm. This nano-morphology can also be observed in all successive cycles of deposition, that is, in NCMS-G2 and NCMS-G3 (see Figure S4a,b, Supporting Information), confirming the robustness and reproducibility of the process. This hierarchical porous structure formed by interconnected nanosheet arrays on the conductive carbon seems ideal for electrolyte ion storage, ensuring access of the electrolytes to the porous structures and reducing the electrolyte ion diffusion path during the battery charge and discharge process, while ensuring electrical percolation and thus good electrochemical performance of the active-material.[22,35] Both deposition steps yield uniform and stable coatings. Figure S5a, Supporting Information, shows that, after EPD of rGO, the surface of the GF is completely covered with thin rGO layers, as evidenced by the increased surface roughness. The average thickness of the rGO layers is less than 80 nm. On the other hand, the CED of 5 CV cycles of MTMSs directly on GF leads to a thicker NiCoMnS$_x$ layer of ≈ 1–1.5 µm, with some irregularities due to the curved structure of the foam (Figure S5b, Supporting Information).[28] To further confirm the sandwich-like interleaved configuration, we performed a cross-section analysis of the NCMS-G2 multilayer sample prepared by cryogenic fracture. Energy dispersive X-ray spectrometry (EDS) line profile analysis provided the relative elemental concentration for each element along with its position in the multilayer. Figure 1d clearly shows the sandwich structure, with two carbon peaks at ≈ 1.8 and 4 µm corresponding to rGO, alternated by areas where carbon is replaced by other atoms (Ni—Co—Mn—S) corresponding nicely to NiCoMnS$_x$ composition. It should be noted that the width of the peaks cannot be used to estimate the rGO thickness as it is much larger than the actual layer thickness due to the complex, tortuous shape of the foam, which does not allow to obtain straight cross sections.

ADVANCED
SCIENCE NEWS
www.advancedsciencenews.com

NANO · MICRO
small
www.small-journal.com
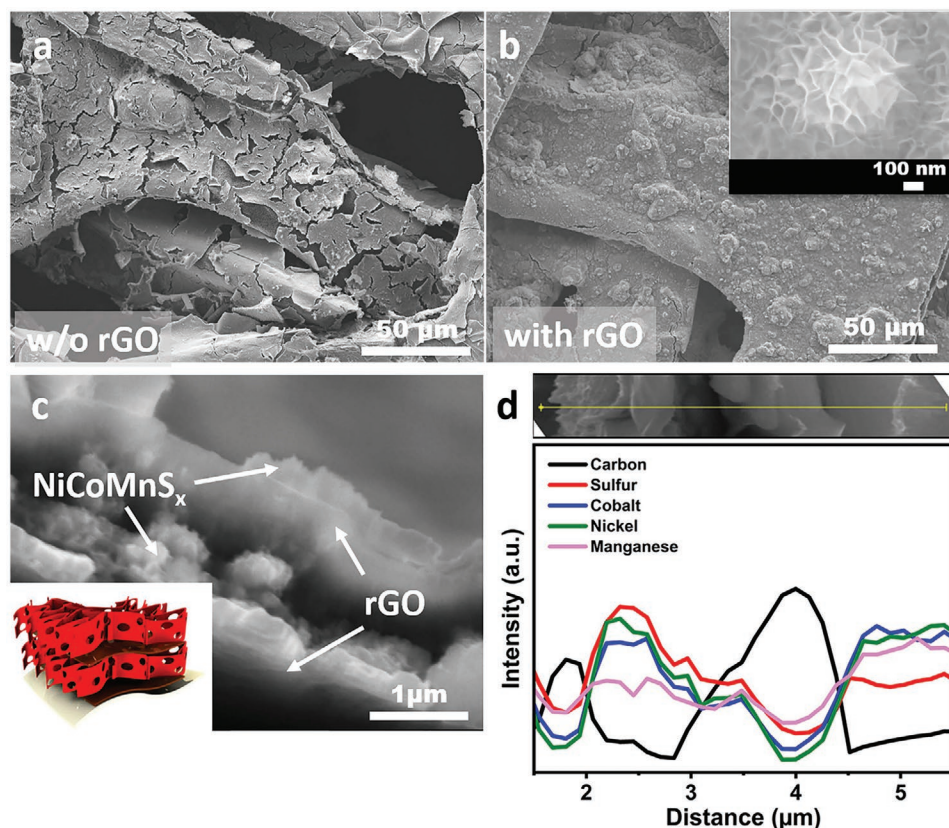
Figure 1. SEM images of a) bulk NCMS (direct growth onto GF). b) NCMS-G1, where the inset shows the SEM image obtained with high magnification. c) Cross-sectional SEM image of NCMS-G2, where the inset shows the schematic representation of the different layers in the sandwich-like structure corresponding to rGO and NCMS indicated by false coloring. The original SEM image with no color is available in Figure S2, Supporting Information. d) SEM Image and Cross-sectional EDS line profile analysis of the NCMS-G2 multilayer sample prepared via cryogenic fracture.

The detailed morphology and composition of the multilayer structure were further studied by Transmission Electron Microscopy **Figure 2**a shows the selected area electron diffraction (SAED) results of the NCMS-G2. The diffraction rings can be indexed to the (220), (200), (422), and (511) crystal planes of the cubic $CoNi_2S_4$ (JCPDS card no. 43-1477) and $NiCo_2S_4$ (JCPDS card no. 20-0782) phases. Figure 2a,b show the low and high magnification TEM images of the NCMS-G2 sample, respectively. The HR-TEM image in Figure 2b shows the lattice fringes with an inter-planar space of 0.186 and 0.261 nm, corresponding to the (511) and (200) planes of the MTMSs structure.

EDS measurements (Figure S6, Supporting Information) reveal that similar amounts of Ni and Co are present in the sample; a small amount of Mn is also detected. This can be expected, given that manganese incorporated into $NiCoS_x$ structures has been observed to electrodeposit poorly under general aqueous conditions when trying to co-deposit multivalent mixed transition metal systems.[36,37] The O signal comes mainly from oxygen functional groups in rGO underlayers and adsorbed oxygen adventitious species while the weak Cl signal comes from the metal chloride precursors employed during the synthesis that are not removed during the washing steps. Figure 2c shows a STEM (scanning transmission electron microscopy)-HAADF (high angle annular dark field) micrograph, and Figure 2d shows its corresponding EDS

spectrometry maps confirming the homogenous distribution of metal cations and sulfur on the carbon network, demonstrating the co-existence of Ni, Co, Mn and S elements.

Figure S7a, Supporting Information, shows XRD data of the different samples; different crystalline phase(s) of the NCMS-G2, NCMS, and rGO can be observed, with peaks attributed to the different crystallographic plane families of cubic phases (Co_3S_4, Ni_3S_2, α-MnS). Test samples produced by using pure NCMS on GF allowed all diffraction peaks to be indexed to different crystallographic plane families of cubic phases indicating their polycrystalline structure: (311), (400), (422), (440), and (511) to the $CoNi_2S_4$ (JCPDS card no. 43-1477), $NiCo_2S_4$ (JCPDS card no. 20-0782) or Co_3S_4 phase (JCPDS 47-1738), (101) to the Ni_3S_2 heazlewoodite phase (JCPDS 98-000-6248), while (200) and (222) belong to the α-MnS phase (JCPDS card No. 88-2223).[6,38,39] Additional diffraction peaks at 26°, 44°, and 55° observed in all samples were correlated to the graphitic carbon matrix (JCPDS 12-0212).[28] Such high crystallinity is noteworthy, given that previous work using electrochemical synthesis methods showed that it is very difficult to obtain highly crystalline samples without additional annealing steps.[22] Raman spectroscopy of pure materials and of multilayer composites further confirmed successful formation of NCMS-GX composites (Figure S7b, Supporting Information). Two peaks centered at 1357 cm^{-1} (D band) and 1582 cm^{-1} (G band), typical of rGO,
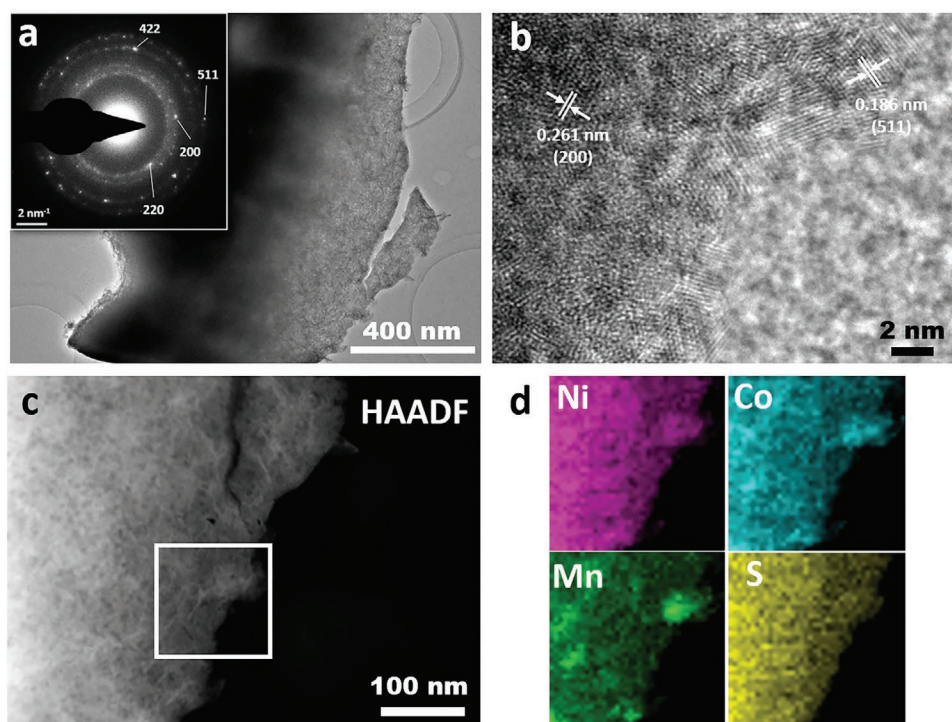
Figure 2. a,b) Low and high magnification TEM images respectively of NCMS-G2; inset shows the selected area electron diffraction (SAED) pattern of the sample, c) STEM-HAADF micrograph of the NCMS-G2 sample. d) STEM-EDSEDS maps of the Ni, Co, Mn, and S elements, within the area marked with a white square in (c).

were observed on all samples, with highest intensity being found on the bare rGO and becoming weaker and weaker on NCMS G1, G2, and G3 samples. Several peaks were observed in the range of 200 to 750 cm^{-1}, which may be attributed to the vibrational modes of M–S (M = Ni, Co, or Mn) bonds, corresponding to that observed in bulk NCMS.[40–42] Overall, all-composite samples showed a combination of similar peaks without significant changes in peak positions in comparison with pure components, confirming that the main structure was retained without any major structural changes despite the formation of the sandwich-like composite.

We used X-ray photoelectron spectroscopy (XPS) to investigate the surface elemental composition and chemical oxidation state of the different metal cations in the NCMS-G2 sandwich-like composite sample.

The XPS survey spectra (Figure S8a, Supporting Information) showed that NCMS-G2 consisted of Ni, Co, Mn, S, O, and C, in which the O signal comes from unavoidable surface oxidation and adsorption of air, while the C signal comes from both GF exposed on the surface and rGO. The S signal is weaker than anticipated from the EDS (Figure S6, Supporting Information). This can be attributed to the low XPS penetration depth into the sample, which leads to a large loss of signal for light elements such as S.[22] XPS measurements are fairly surface sensitive (outermost 2–10 nm of a solid surface).[43]

The chemical valence of each element was analyzed by fitting the high-resolution XPS spectra using the Gauss–Lorentz fitting method. **Figure 3**a–d shows the typical Ni 2p, Co 2p, Mn 2p, and S 2p core levels of the NCMS-G2 sample. The

Ni 2p and Co 2p core-level spectra can be well-fitted with two spin-orbit splitting which is characteristic of Ni^{2+}/Ni^{3+} and Co^{2+}/Co^{3+}, respectively, and two shakeup satellites (denoted as "Sat."). Figure 3a shows that the binding energies of Ni 2p peaks located at 855.2 and 872.7 eV correspond to Ni 2p$_{3/2}$ and Ni 2p$_{1/2}$, respectively.[44] Similarly, for the Co 2p XPS spectrum in Figure 3b, the peaks at 780.6 and 796.6 eV are related to Co 2p$_{3/2}$ and Co 2p$_{1/2}$, respectively. The intensity of the fitted peaks and the weak satellites indicate that Co^{3+} is the dominant state of Co near the surface of the sample.[45] Moreover, Figure 3c displays two peaks at a binding energy of 641.2 and 652.9 eV, corresponding to Mn 2p$_{3/2}$ and Mn 2p$_{1/2}$ with a strong splitting of 6.0 eV (closer to the value of Mn^{2+}/O (5.9 eV)) in the Mn 3s core level (shown in Figure S8b, Supporting Information), which reveal that Mn^{2+} species are dominant on the surface of the sample, probably due to a high degree of manganese surface oxidation.[46] The sulfur content in the NCMS-G2 sample surface can also be confirmed by the XPS analysis whose results are illustrated in Figure 3d. The S 2p spectrum can be divided into two main peaks located at 161.4 and 163.0 eV corresponding to S 2p$_{3/2}$ and S 2p$_{1/2}$, respectively. The S 2p peak noticed at 167.8 eV can be attributed to surface sulfur with high oxidation state, S-O bonding, coming from sulfoxide (SO$_x$), easily formed on the surface of sulfide materials.[35,47] Therefore, according to the XPS analysis, the near-surface of the NCMS-G2 sample contains Ni^{2+}, Ni^{3+}, Co^{2+}, Co^{3+}, Mn^{2+}, and S^{2-}. These results are in good agreement with earlier reports of the chemical states of Ni, Co, and Mn ternary and binary MTMSs.[18,24,48]
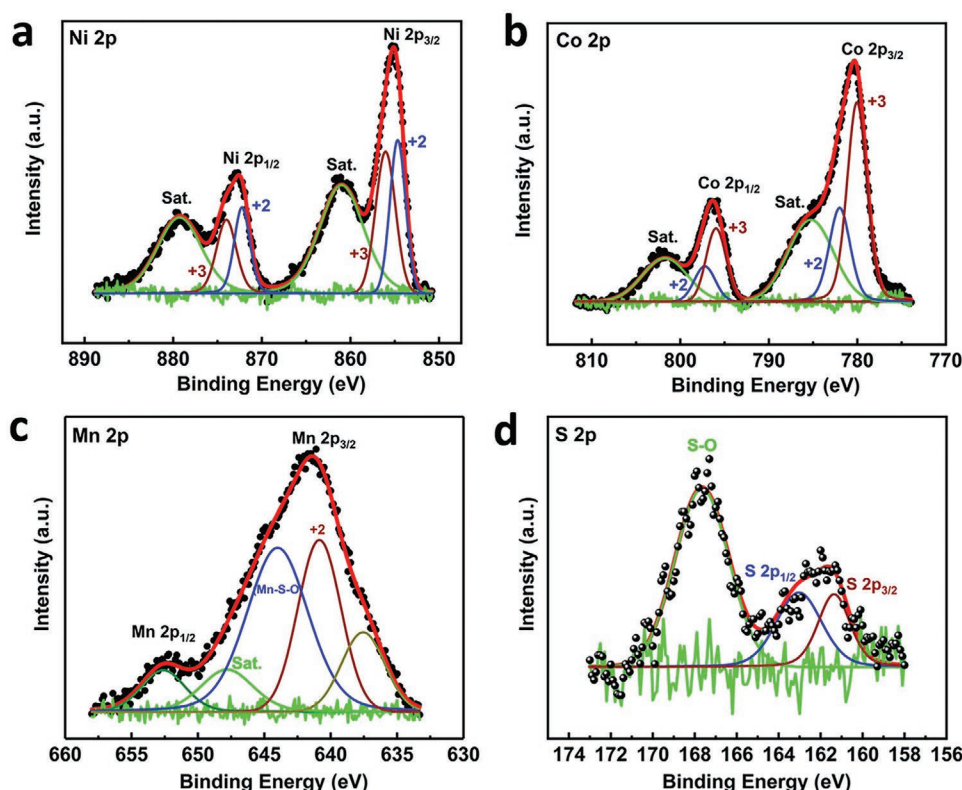
Figure 3. XPS surface analysis of the NCMS-G2 sandwich-like structure: a) Ni 2p, b) Co 2p, c) Mn 2p, and d) S 2p core levels. Shakeup satellites are indicated as "Sat."

2.2. Electrochemical Characterization of the Samples

Figure 4a and Figure S11a show the CV curves of the NCMS-GX multilayer samples in 3M KOH, with X being 1,2,3 stacked layers of rGO and NCMS. The CV is compared to that of bulk NCMS and rGO samples directly grown on GF. Scan rate was 2 mV s^{-1}. The CV shapes clearly reveal the Faradaic characteristics of the sulfide samples with a battery-type signature, while the rGO sample shows a capacitive behavior, being non-redox-active in that specific potential window (0–0.6 V). The specific peak current intensity increased remarkably in all composite samples if compared with pristine NCMS (black curve), thereby providing a significant improvement in energy storage capability of the samples. This can be attributed to favorable distribution of NCMS nanosheets on conducting rGO layers, which facilitates the electron and ion transfer compared to the direct electrodeposition of NCMS on GF resulting in cracks and delamination (as seen in Figure 1a,b). Figure S9, Supporting Information, shows the CV curves of the NCMS-G2 electrode at various scan rates from 2 to 20 mV s^{-1}. The CV curves show a pair of redox peaks caused by the redox reaction of transition metal ions with the OH$^-$. In accordance with the CV results, the potential plateaus between 0.25 and 0.4 V in galvanostatic charge–discharge profiles at 1 A g^{-1} corroborated the faradaic nature of the charge storage process, maintaining a stable profile shape as the current densities increased (see Figure 4b,c). Moreover, Figure 4b shows nearly symmetric charge and discharge curves suggesting excellent reversibility of redox reactions and good

coulombic efficiency in all the samples. In good agreement with CV analysis, the NCMS-G2 electrode (red curve) showed significantly higher specific capacity (192 mAh g^{-1}) in comparison with that of the pure NCMS (black curve) (114 mAh g^{-1}) and the other multilayer structures (150 and 178 mAh g^{-1} for NCMS-G1 and NCMS-G3, respectively) (Figure 4b). Moreover, the overpotential of bulk NCMS and NCMS-G3 is slightly higher than for NCMS-G1 and NCMS-G2, suggesting better transport properties in the latter two samples.

Figure 4c shows charge–discharge profiles of NCMS-G2 at increasing current densities confirming the excellent rate capability of this multilayer electrode that shows similar values of specific capacity and low overpotentials when the current is 10 times higher. For higher currents (>10 A g^{-1}), the specific capacity and overpotential increase is likely due to transport limitation at such high currents. For the sake of comparison, Figure S10a, Supporting Information, shows the charge–discharge profiles at 1 A g^{-1} of the ternary NCMS$_x$ versus the binary metal sulfide NCS$_x$ synthesized in a similar way. The comparison demonstrates the important role of Mn ions in NiCo$_2$S$_4$ to activate the 3d electrons of Co on the (110) surface and provide enhanced affinity for OH, improving rate capability (see Figure S10b, Supporting Information) and electrochemical energy storage, as previously demonstrated by Chen et al.[49] For comparison sake, we also tested pure rGO electrodes, which showed a quasi-triangular shape typical of capacitor-type materials, with almost no capacity contribution, as we expected, in good agreement with CV experiments (Figure S10c,d, Supporting Information).
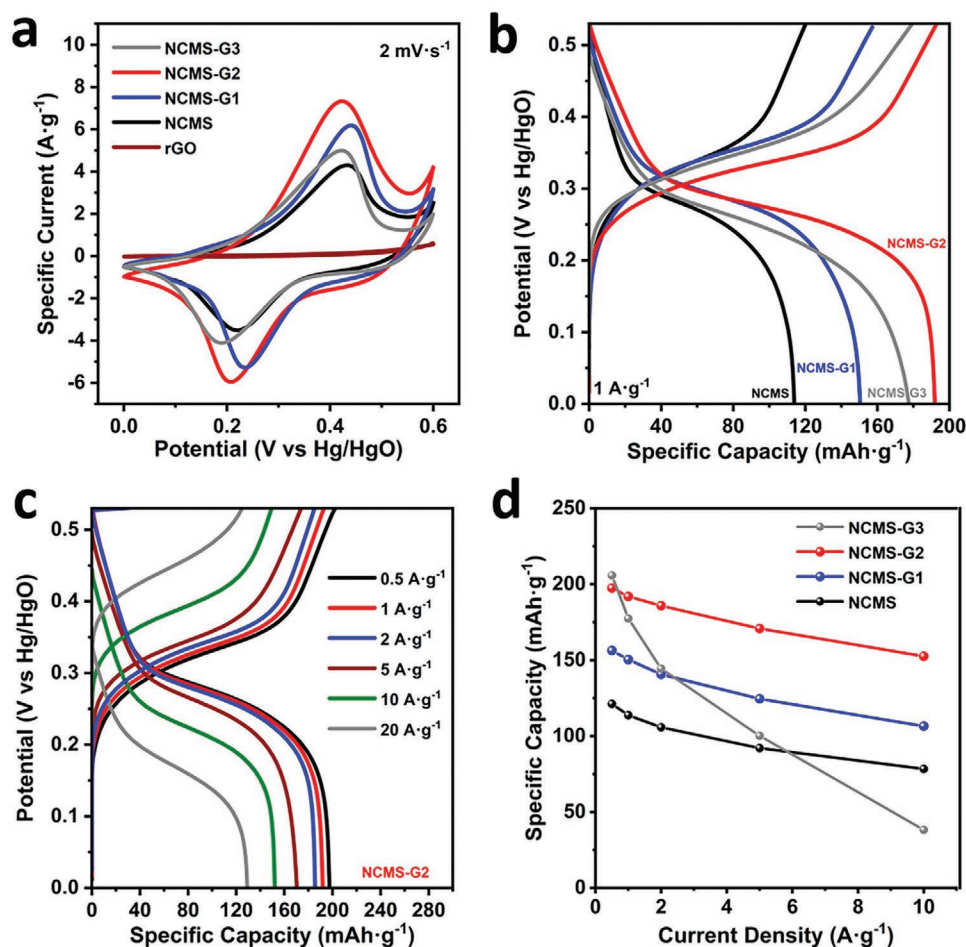
Figure 4. Electrochemical tests of the NCMS-G*X* multilayer samples and NCMS samples as battery-type electrode materials in 3 M KOH solution: a) CV curves of the NCMS-GX multilayer materials and pure NCMS sample at a scan rate of 2 mV s⁻¹, b) charge–discharge profiles of the NCMS-GX multilayer samples at 1 A g⁻¹, c) charge–discharge profiles of the NCMS-G2 multilayer sample at various current densities, and d) rate capability of the samples at various current densities.

The specific capacities of the NCMS, NCMS-G1, NCMS-G2, and NCMS-G3 samples were determined from the charge–discharge curves at different current densities (Figure 4d). A general trend was evident at lower current densities, where samples with an increasing number of layers (G1, G2, G3) gave an increasing specific capacity (156.4 mAh g⁻¹, 197.5 mAh g⁻¹, and 205.8 mAh g⁻¹, respectively at 0.5 A g⁻¹), as also detected in rate capability based on calculated areal capacities (Figure S11, Supporting Information). However, when the current range increased (i.e., 10 A g⁻¹), the NCMS-G2 sample showed the larger specific capacity (152.6 mAh g⁻¹, 77% capacity retention) while the NCMS-G3 sample exhibited a significant drop in its specific capacity, going down to 38.3 mAh g⁻¹ (18% capacity retention). This decay can be explained by the agglomerated layers or nanosheet distribution shown in the SEM images of the NCMS-G3 in Figures S2c and S4b, Supporting Information, that might cause electronic conductivity limitations, in particular for thicker electrodes like NCMS-G3, formed by three stacked layers of metal sulfides and rGO. On the other hand, the excellent rate behavior of NCMS-G2 indicates that its porous, interconnected nanosheet arrays provide sufficient

diffusion channels for the rapid redox reaction of electrolyte ions, without blocking channels or causing nanosheet agglomeration on the structure. It is noteworthy that the electrochemical performance of our NCMS-G2 multilayer electrode was comparable or superior to previously published, nanostructured mixed metal oxides/sulfides and their composite materials, even those on metallic substrates such as Ni foam (see Table S1, Supporting Information, for a detailed comparison). The influence of electrical conductivity on the performance of multilayer electrodes was studied using electrochemical impedance spectroscopy (EIS) measurements. Figure S12, Supporting Information, shows a Nyquist plot obtained in the frequency range of 200 kHz–0.1 Hz at an open circuit potential. As observed in Figure S12, Supporting Information, inset, the x-axis intercept in the high-frequency region is the equivalent series resistance, *R*ₛ, related to that of the electrode material and the bulk resistance of the electrolyte. NCMS-G2 yielded 1.53 Ω, but the other multilayer samples and bare NCMS exhibited a small increase in their *R*ₛ, similar in all cases and close to 2 Ω. Moreover, in the semicircle corresponding to the charge transfer resistance (*R*ct), the lowest value corresponds to the NCMS-G2 sample. These

results suggest that NCMS-G2 electrode has an optimal balance between high loading of active material and efficient electron and/or ion transfer during the charge–discharge process.

To better understand the origin of such excellent performance, we compared the CV signal of NCMS-G2 with NCMS-G1*, a sample made with 10 cathodic CV cycles of NCMS deposition, but only one initial coating step of rGO (see Figure S13a, Supporting Information). Both electrodes have a very thick sulfide coating of a few microns (see also Figure S3, Supporting Information), but NCMS-G2 has a thin interlayer of rGO between the sulfide coatings. The NCMS-G1* sample without rGO as interlayer showed a very low performance, explained by the formation of cracks, visible in Figure S3. In summary, the CV of Figure S13a, Supporting Information, demonstrates the utility of using rGO layers as porous spacers and/or stabilizers, to increase electrical conductivity and protect sulfides against delamination and agglomeration, therefore improving the overall electrochemical performance of the sample in all current ranges, as demonstrated in Figure S13b.

2.3. Performance of the Multilayers in an RAB

After demonstrating the good performance of the NCMS-G2 cathode, we also tested a full device, combining the cathode with an appropriate anode to achieve a high-performing aqueous RAB.

For best performance, we used an advanced anode consisting of an anthraquinone-based conjugated microporous polymer (referred to as IEP-11 for simplicity) that features a robust 3D structure, high specific surface area, and combination of micro/meso porosities. As we demonstrated previously, these characteristics are beneficial to achieve concurrent high specific capacity, rate capability, and ultra-long cyclability in Li-ion half cells.[50,51] In this work, we combined the IEP-11 anode with the innovative NCMS-G2 cathode in alkaline rechargeable batteries. Complete electrochemical characterization of IEP-11 in a three-electrode configuration shows that this conjugated redox polymer exhibits a suitable low redox reaction potential to accommodate K^+ at $\approx$ −0.7 V versus Hg/HgO (Figure S14a, Supporting Information). Moreover, IEP-11 also shows excellent reversibility and fast kinetics with high specific capacity values of 91 mAh g^{-1} at 0.5 A g^{-1} and 60 mAh g^{-1} at current densities as high as 20 A g^{-1} (Figure S14b,c, Supporting Information). According to the individual CV and charge–discharge curves of the IEP-11 anode and optimized NCMS-G2 cathode obtained in the three-electrode configuration (see Figure S15a,b, Supporting Information), the operating voltage window of a battery combining these two electrodes was found to be 1.6 V with a theoretical open-circuit voltage as high as 1.1 V.

We then assembled NCMS-G2//IEP-11 full cell aqueous rechargeable batteries, and evaluated their electrochemical performance. The optimal cathode/anode mass ratio was found to be 0.45, see SI for calculation details. The behavior of the individual electrodes in the full cell was monitored via a Hg/HgO reference electrode placed in a T-shape Swagelok cell at a discharge current density of 1 A g^{-1} to ensure that the charge of electrodes was well balanced by adjusting the mass of electrodes. The curves for positive and negative electrodes
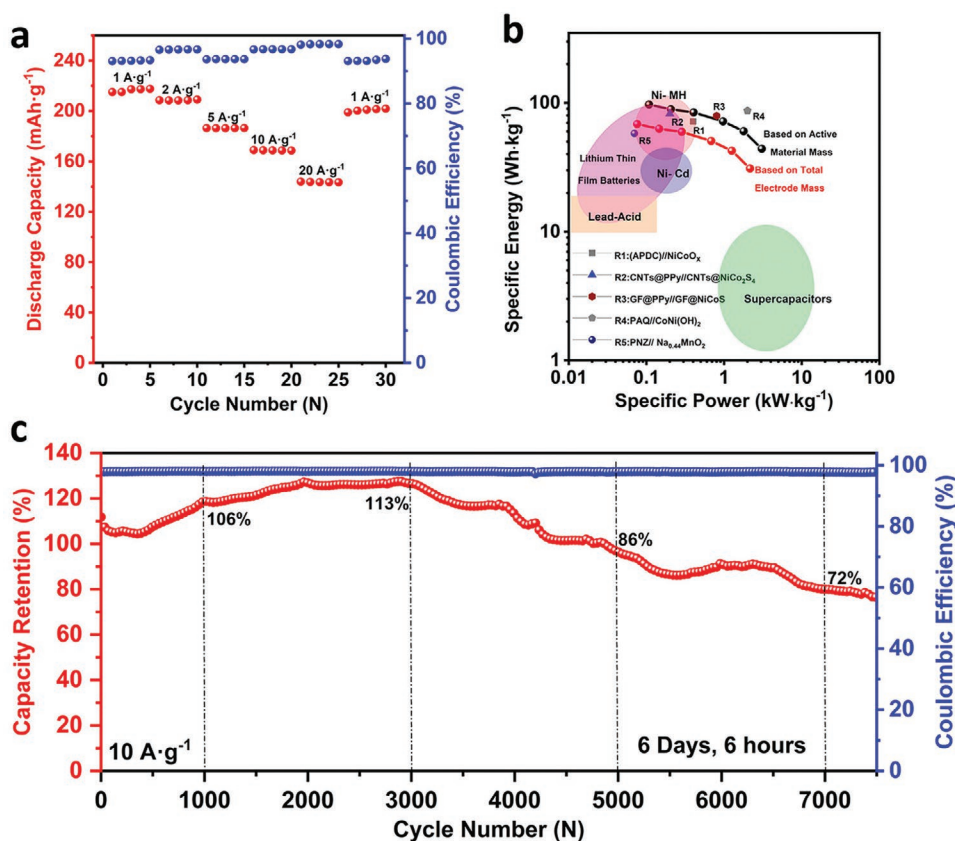
(Figure S16, Supporting Information) showed that the behavior of each electrode in the full cell was similar to what was already observed in the three-electrode system. This confirmed that the mass of electrodes is reasonably well-balanced for good performance in the selected potential region.

Initially, the battery was charged/discharged at constant current densities of 1, 2, 5, 10, and 20 A g^{-1} and the obtained voltage profiles are provided in Figure S15c, Supporting Information. The corresponding capacities were 218, 209, 186, 169, and 144 mAh g^{-1} (66% capacity retention, after a 20-fold increase in current density) based on the total cathode mass of NCMS-G2 (3.8 mg cm^{-2}) as shown in **Figure 5**a.

Specific energy and specific power are two key performance indicators for a practical battery. The NCMS-G2//IEP-11 RAB compared positively with previously published polymer/metal oxide-sulfide batteries (Table S2, Supporting Information) such as $(APDC)//NiCoO_X$ (71.7 Wh kg^{-1} at 0.4 kW kg^{-1}), $CNTs@PPy//CNTs@NiCo_2S_4$ (82.4 Wh kg^{-1} at 0.2 kW kg^{-1}), $GF@PPy//GF@NiCoS$ (79.3 Wh kg^{-1} at 0.80 kW kg^{-1}), poly(anthraquinone)//$CoNi(OH)_2$ (87 Wh kg^{-1} at 2 kW kg^{-1}) and phenazine//$Na0.44MnO_2$ (58 Wh kg^{-1} at 0.07 kW kg^{-1}).

Published performance indicators can be sometimes misleading because they calculate performance on the mass of the active material, and not the mass of the electrode. To be fair, we constructed a Ragone plot (Figure 5b) calculating specific energy and specific power in two ways, one based on the active material mass (black line); and the other based on the whole electrode mass (red line) (detailed calculations are presented in the Supporting Information). By considering only the total mass of active materials, our NCMS-G2//IEP-11 battery delivers a maximum specific energy of 97.2 Wh kg^{-1} at 108 W kg^{-1}. Even more promisingly, at a high-specific power of 3.1 kW kg^{-1}, a high specific energy of 44 Wh kg^{-1} can still be achieved demonstrating the excellent rate capability of the battery. It is worth noting that when the total electrode mass of the cell is considered, the use of a lightweight GF current collector in the cathode and a metal current collector-free rGO+SWCNTs buckypaper anode in our full cell yields an unprecedented gravimetric energy density of 68.5 Wh kg^{-1}. This value is almost seven times higher than that of typical commercial SCs, much higher than that of Ni/Cd or lead–acid Batteries, and similar to that of Ni-MH Batteries. The maximum power density is 2.2 kW kg^{-1}, which is comparable to that of commercial SCs and five times higher than that of lithium thin-film batteries.[10] These values at the electrode level definitely highlight the suitability of our battery for energy storage applications, particularly where both weight and energy/power parameters are crucial.

Temperature dependence is also important for evaluating the performance of RABs, especially for their low-temperature operation. The NCMS-G2//IEP-11 full cell demonstrated 83% capacity retention at a rather low temperature of −30 °C compared to its capacity at +25 °C (Figure S17, Supporting Information), indicating low-temperature dependence due to the excellent low-temperature performance of both active materials in the cathode and anode. For the sake of comparison, commercial Nickel-metal hydride (NiMH) batteries deliver only 50% of their nominal energy at −25 °C, once again suggesting better low-temperature performance of our cell.[52] Figure 5c and Figure S18, Supporting Information, show the cycling

**ADVANCED
SCIENCE NEWS**

www.advancedsciencenews.com

**NANO · MICRO
small**

www.small-journal.com

Figure 5. Electrochemical performance of an NCMS-G2//IEP-11 RAB: a) rate capability of the RAB at various current densities, b) Ragone plot of the RAB at various current densities, and c) cycling performance of the RAB at 10 A g^{-1}.

performance of the NCMS-G2//IEP-11 full cell at 10 and 1 A g^{-1}, respectively. In both cases, we observed phases of activation and stabilization of the cell during functioning. This interesting performance might be attributed to the electro-activation of the electrode–electrolyte interface and significant increase in accessible active sites for the electrolyte due to the sandwich-like layered composite structure.[18] After 7000 cycles at 10 A g^{-1} (Figure 5c) our full cell was able to retain 72% of its initial capacity, while at 1 A g^{-1} cycling for more than 10 days and 1100 cycles, the cell was able to retain 79% of the initial capacity with coulombic efficiencies close to 100% in all cases. The post mortem SEM images of the NCMS-G2 cathode (Figure S19, Supporting Information) fully confirm the structural and morphological integrity of the hierarchical multilayer structure after long cycling. This overall performance in terms of concurrent ultra-long cycling stability, unprecedented high energy density for an alkaline rechargeable battery, and large power in the range of SCs is far superior to any previously reported RABs.

3. Conclusions

In summary, we demonstrated a new synthetic route combining electrochemical methods to create complex hierarchical electrodes made of multilayers of vertically aligned NiCoMnS nanosheet arrays, alternated with horizontal spacers of reduced graphene oxide, rGO, all deposited on a 3D conductive GF. The

combination of EPD and CED has been already used in previous works to co-deposit different materials. Here, by careful tuning of the deposition chemistry, we could though achieve a truly multilayered structure, where the different layers have a different but controlled composition, demonstrating that this electrochemical method is fully tunable and has several advantages over the conventional processes for the preparation of mixed metal oxides/sulfide composites: low-cost, facile upscaling and improved synthetic design to host a large number of reactive sites by sandwiching the electrode. By properly optimizing the EPD time, temperature of CED, and number of layers alternately deposited, we achieved a top performance of 197.5 mAh g^{-1} at 0.5 A g^{-1}, and 66% of capacity retention after a 20-fold increase in specific current at 20 A g^{-1}. The optimized NCMS-G2 electrode was employed as a cathode in the assembly of a full RAB of 1.60 V, integrated with an anthraquinone-based redox-active conjugated microporous polymer electrode as anode. It had maximum specific energy of 97.2 Wh kg^{-1} and a maximum power density of 3.1 kW kg^{-1} based on the total mass of active materials, with an excellent long-term cycling stability of 72% over 7000 cycles at 10 A g^{-1}. These results suggest that this combination of a high-rate conjugated microporous polymer as anode and a high capacity multilayer NCMS-G2 cathode is an extremely robust match for assembling high-performance RAB. We should underline that energy densities close to 100 Wh kg^{-1} in a RAB have not been reported in the literature to date. We predict that the versatility of such a

**ADVANCED
SCIENCE NEWS**
www.advancedsciencenews.com

**NANO · MICRO
small**
www.small-journal.com

multilayer and low-cost electrochemical synthesis approach is not limited to the specific material reported and could allow the fabrication of other multilayer graphene/sulfides/oxides/2D material sandwich-like structures for various energy storage technologies. Furthermore, these results also pave the way towards next-generation electrochemical coatings on different conductive or porous substrates, highly requested for a wide range of industrial applications such as anticorrosion, electrochemical sensors, or gas barrier systems.

4. Experimental Section

All the reagents used for synthesis and experiments were analytical grade and employed as received, without any further purification. Distilled milli-Q water was used in all the experiments. GO was prepared by oxidizing natural graphite powder (Sigma Aldrich, <20 μm, San Luis, USA) according to a modified Hummers' method,[53,54] followed by a chemical reduction with hydrazine monohydrate to ensure that GO was dominantly converted to its reduced state (rGO).[55]

Preparation of 3D GF: Nickel foams were used as the 3D templates for CVD graphene growth. A piece of Ni foam (60 × 30 mm) was washed thoroughly by ultra-sonication in dilute HCl (3 wt%), DI water, and acetone successively, to remove the contaminants. It was placed in a standard quartz tube furnace and heated up to 1000 °C under H_2 (50 s.c.c.m.) gas flow, and then annealed for 30 min. to clean the surface and remove the thin nickel oxide layer. Then, CH_4 was introduced into the tube with low concentration (50 s.c.c.m) while the H_2 flow was increased to 500 s.c.c.m. for 10 min. growth time. The sample was quickly cooled to room temperature with a cooling rate of approximately 100 °C min^{-1} under an argon atmosphere. The prepared sample was immersed in a $FeCl_3$ (4.5 wt% in DI water) solution at 80 °C overnight, and then etched in 10 wt% HCl for 4 h at 80 °C, to completely remove the nickel metal and salt residues.
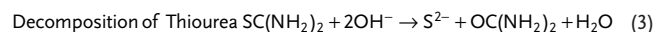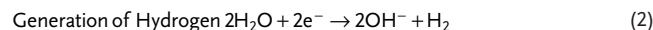
EPD of rGO on GF: 20 mg of rGO powder was dispersed in 50 mL of *N,N'*-dimethylformamide (DMF) by using a Hielscher UP400S ultrasonic liquid processor for 20 min. The negative surface charge of rGO particles in DMF solution[56] was modified by slowly adding 500 μL of poly diallyldimethylammonium chloride (PDADMAC; 20 wt% in H_2O Sigma Aldrich) dissolved in a small amount (1 mL) of EtOH with the help of a batch sonicator. PDADMAC was a cationic polymer industrially used to tune the surface charge of particles, as a fixation agent or a flocculant, also used in one of the recent works.[26] By mixing small amounts of PDADMAC with the rGO suspension, the quaternary cations adsorbed on the rGO surface.[57] Then, the authors immersed the GF in the above-mentioned suspension, and the deposition proceeded through cathodic electrophoresis. The approach was different from EPD in the conventional aqueous suspension, the latter being prone to cause oxidative damage to the GF via the electrolysis of water (see Scheme 1). The working electrode (WE) consisted of a 30 × 10 mm (length × width) GF, while a Pt mesh (40 × 15 mm) served as a counter electrode (CE) located parallel to the GF at a distance of 40 mm. The EPD was observed only on the WE, while no deposition was observed on the CE, confirming that the electric field was acting on positively charged particles. Optimal EPD conditions were achieved by applying a DC potential of −20 V for 10 min. An EPD time optimization study was performed before selection (Figure S20a, Supporting Information) using −20 V as ideal voltage for precise control of the amount of material deposited, creating a thin layer of rGO of ≈0.33 mg cm^{-2}. After the coating, the electrodes were dried at 70 °C for 30 min.

CED of NCMS Nanostructures: Owing to the chemical inertness and hydrophobic nature of the CVD graphene surface, it was extremely difficult to obtain a uniform film of metal compounds through their electrochemical deposition. To circumvent the surface adhesion issues, a thin layer of rGO on CVD-GF is first coated. Therefore, a piece of GF (30 × 10 mm) pre-coated with

rGO was immersed in a water/EtOH (1:1 volume ratio) solution[28] containing three metal salts: 10 mM $NiCl_2\cdot6H_2O$, 10 mM $CoCl_2\cdot6H_2O$, 20 mM $MnCl_2\cdot6H_2O$, and 0.1 M thiourea as sulfur source at room temperature. This solution was bubbled with Ar until saturation, ≈30 min prior to the CV electrodeposition. Electrodeposition of NCMS nanostructures was performed with a three-electrode system via CV, where the 3D rGO-GF was used as the WE, a platinum mesh as the CE located parallel to the rGO-GF at a distance of 40 mm and an Ag/AgCl as the RE, (see Scheme 1). Prior to the electrodeposition on GF, a temperature optimization study was performed on Ni foam, observing no benefits by increasing temperature to 75 °C in a three-electrode capacity study. (Figure S20b, Supporting Information). The mass of NCMS deposited was controlled by adjusting the number of CV cycles.[58] The optimal CV cycles carried out were five, corresponding to an approximate mass loading of 2 mg cm^{-2}. Electrodeposition was performed over the course of 1 h at a scan rate of 5 mV s^{-1} between −1.2 V and 0.3 V (see Figure S21b, Supporting Information), and approximately five NCMS layers were observed to form, corresponding to the five CV cycles performed on the rGO-GF surface (Figure S22, Supporting Information). The electrodeposition method was an attractive way to grow MTMSs on conductive substrates through the cathodic reduction reaction with controlled composition and film thickness. After coating, the electrodes were dried at 70 °C for 1 h. The voltammograms exhibit broad oxidation and reduction peaks centered at 0.2 and −0.50 V, respectively (see Figure S21b, Supporting Information). These peaks were attributed to the one-electron oxidation of thiourea to formamidine disulfide and its corresponding reduction according to the following mechanism already reported in literature:[59,60]

$$2[SC(NH_2)_2] \rightarrow \left[SC(NH)NH_2\right]_2 + 2H^+ + 2e^- \qquad (1)$$
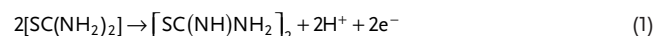
The peak current increases on repeated cycling. The overall reactions involved in the deposition of the NCMS films are given below:

$$\text{Generation of Hydrogen } 2H_2O + 2e^- \rightarrow 2OH^- + H_2 \qquad (2)$$

$$\text{Decomposition of Thiourea } SC(NH_2)_2 + 2OH^- \rightarrow S^{2-} + OC(NH_2)_2 + H_2O \qquad (3)$$

$$\text{Formation of MTMS } Ni^{2+} + Co^{2+} + Mn^{2+} + xS^{2-} \rightarrow NiCoMnS_x \qquad (4)$$

Bi and tri-layers of NCMS and rGO coating were obtained by repeating alternately the previous steps (4.2 and 4.3), creating novel multilayer composites of NCMS-G*X*, where *X* is the number of alternately deposited layers of rGO and NCMS. The final mass loading of the electrode was ≈2.8 mg cm^{-2} for the sample NCMS-G1, ≈3.7 mg cm^{-2} for the sample NCMS-G2 and ≈5 mg cm^{-2} for the sample NCMS-G3, with an average sulfide to carbon weight ratio of 8:2 in all cases. For sake of comparison, pure NCMS on GF and rGO on GF samples were also synthesized using the same procedure, including no rGO in the pure sulfide sample and no metal precursors+thiourea in the rGO sample. Moreover, NCMS-G1* with 10 CV cathodic electrodeposited cycles of MTMSs (≈3.7 mg cm^{-2}) was also synthesized to demonstrate the role of rGO as a conductive interlayer material in the multilayer electrodes. Each sample was produced and characterized twice, and each electrochemical measurement was repeated 5 times/cycles.

The Experimental details for the microstructural and electrochemical measurements can be found in the ESI.

Preparation of Polymer-Based Anode Material: A hybrid anthraquinone-based conjugated microporous polymer containing rGO and single-walled carbon nanotubes (SWCNTs) (90/5/5 wt %) (IEP-11@R5S5, named as IEP-11 for simplicity) was synthesized via Sonogashira cross-coupling polymerization with combined miniemulsion and solvothermal approaches as reported in the previous publication.[51] Next, the SWCNT-assisted buckypaper approach was used to obtain self-supported, binder and metal collector free electrodes as reported.[51]

**ADVANCED
SCIENCE NEWS**

www.advancedsciencenews.com

**NANO · MICRO
small**

www.small-journal.com

Supporting Information

Acknowledgements

Conflict of Interest

The authors declare no conflict of interest.

Data Availability Statement

The data that support the findings of this study are available from the corresponding author upon reasonable request.

Keywords

[1] D. Larcher, J. M. Tarascon, *Nat. Chem.* **2015**, *7*, 19.
[2] S. Few, O. Schmidt, G. J. Offer, N. Brandon, J. Nelson, A. Gambhir, *Energy Policy* **2018**, *114*, 578.
[3] J. Lu, Z. Chen, Z. Ma, F. Pan, L. A. Curtiss, K. Amine, *Nat. Nanotechnol.* **2016**, *11*, 1031.
[4] S. Zheng, Y. Sun, H. Xue, P. Braunstein, W. Huang, H. Pang, *Natl. Sci. Rev.* **2021**, https://doi.org/10.1093/nsr/nwab197.
[5] Y. Bai, C. Liu, T. Chen, W. Li, S. Zheng, Y. Pi, Y. Luo, H. Pang, *Angew. Chem., Int. Ed.* **2021**, *60*, 25318.
[6] M. G. Park, J. W. Choi, I. W. Ock, G. H. Kim, J. K. Kang, *Adv. Energy Mater.* **2021**, *11*, 2003563.
[7] A. Kwade, W. Haselrieder, R. Leithoff, A. Modlinger, F. Dietrich, K. Droeder, *Nat. Energy* **2018**, *3*, 290.
[8] J. Meng, H. Guo, C. Niu, Y. Zhao, L. Xu, Q. Li, L. Mai, *Joule* **2017**, *1*, 522.
[9] J. Li, H. Zhao, J. Wang, N. Li, M. Wu, Q. Zhang, Y. Du, *Nano Energy* **2019**, *62*, 876.
[10] J. Liu, M. Chen, L. Zhang, J. Jiang, J. Yan, Y. Huang, J. Lin, H. J. Fan, Z. X. Shen, *Nano Lett.* **2014**, *14*, 7180.
[11] C. Yuan, H. Bin Wu, Y. Xie, X. W. Lou, *Angew. Chem., Int. Ed.* **2014**, *53*, 1488.
[12] J. S. Sanchez, A. Pendashteh, J. Palma, M. Anderson, R. Marcilla, *Electrochim. Acta* **2018**, *279*, 44.
[13] J. S. Sanchez, A. Pendashteh, J. Palma, M. Anderson, R. Marcilla, *ChemElectroChem* **2017**, *4*, 1295.
[14] J. Liu, C. Guan, C. Zhou, Z. Fan, Q. Ke, G. Zhang, C. Liu, J. Wang, *Adv. Mater.* **2016**, *28*, 8732.
[15] D. Lei, D. C. Lee, A. Magasinski, E. Zhao, D. Steingart, G. Yushin, *ACS Appl. Mater. Interfaces* **2016**, *8*, 2088.
[16] F. Sun, Q. Li, Y. Bai, G. Zhang, S. Zheng, M. Peng, X. Chen, N. Lin, H. Pang, *Chinese Chemical Letters* **2021**, https://doi.org/10.1016/j.cclet.2021.10.075.
[17] X. Y. Yu, X. W. Lou, *Adv. Energy Mater.* **2018**, *8*, 1701592.
[18] J. S. Sanchez, A. Pendashteh, J. Palma, M. Anderson, R. Marcilla, *J. Mater. Chem. A* **2019**, *7*, 20414.
[19] P. Geng, S. Zheng, H. Tang, R. Zhu, L. Zhang, S. Cao, H. Xue, H. Pang, *Adv. Energy Mater.* **2018**, *8*, 1703259.
[20] Y. Zhao, L. P. Wang, M. T. Sougrati, Z. Feng, Y. Leconte, A. Fisher, M. Srinivasan, Z. Xu, *Adv. Energy Mater.* **2017**, *7*, 1601424.
[21] A. K. Geim, K. S. Novoselov, *Nat. Mater.* **2007**, *6*, 183.
[22] C. Zhang, X. Cai, Y. Qian, H. Jiang, L. Zhou, B. Li, L. Lai, Z. Shen, W. Huang, *Adv. Sci.* **2018**, *5*, 1700375.
[23] G. He, M. Qiao, W. Li, Y. Lu, T. Zhao, R. Zou, B. Li, J. A. Darr, J. Hu, M. M. Titirici, I. P. Parkin, *Adv. Sci.* **2017**, *4*, 1600214.
[24] A. Pendashteh, J. S. Sanchez, J. Palma, M. Anderson, R. Marcilla, *Energy Storage Mater.* **2019**, *20*, 216.
[25] M. F. Iqbal, M. N. Ashiq, M. Zhang, *Energy Technol.* **2021**, *9*, 2000987.
[26] J. S. Sanchez, J. Xu, Z. Xia, J. Sun, L. E. Asp, V. Palermo, *Compos. Sci. Technol.* **2021**, *208*, 108768.
[27] Z. Y. Xia, D. Wei, E. Anitowska, V. Bellani, L. Ortolani, V. Morandi, M. Gazzano, A. Zanelli, S. Borini, V. Palermo, *Carbon* **2015**, *84*, 254.
[28] Z. Y. Xia, M. Christian, C. Arbizzani, V. Morandi, M. Gazzano, V. Quintano, A. Kovtun, V. Palermo, *Nanoscale* **2019**, *11*, 5265.
[29] A. B. Artyukhin, O. Bakajin, P. Stroeve, A. Noy, *Langmuir* **2004**, *20*, 1442.
[30] W. Tian, A. VahidMohammadi, Z. Wang, L. Ouyang, M. Beidaghi, M. M. Hamedi, *Nat. Commun.* **2019**, *10*, 2558.
[31] M. Wang, J. Oh, T. Ghosh, S. Hong, G. Nam, T. Hwang, J. D. Nam, *RSC Adv.* **2014**, *4*, 3284.
[32] Z. Li, J. Wang, X. Liu, S. Liu, J. Ou, S. Yang, *J. Mater. Chem.* **2011**, *21*, 3397.
[33] Z. Chen, W. Ren, L. Gao, B. Liu, S. Pei, H. M. Cheng, *Nat. Mater.* **2011**, *10*, 424.
[34] M. Xu, H. Guo, R. Xue, M. Wang, N. Wu, X. Wang, J. Zhang, T. Zhang, W. Yang, *J. Alloys Compd.* **2021**, *863*, 157699.
[35] W. Chen, C. Xia, H. N. Alshareef, *ACS Nano* **2014**, *8*, 9531.
[36] F. H. Assaf, M. M. Abou-Krisha, O. K. Alduaij, A. M. A. El-Seidy, A. A. Eissa, *Int. J. Electrochem. Sci.* **2015**, *10*, 6273.
[37] M. W. Glasscott, A. D. Pendergast, S. Goines, A. R. Bishop, A. T. Hoang, C. Renault, J. E. Dick, *Nat. Commun.* **2019**, *10*, 2650.
[38] Y. Ma, Y. Ma, G. T. Kim, T. Diemant, R. J. Behm, D. Geiger, U. Kaiser, A. Varzi, S. Passerini, *Adv. Energy Mater.* **2019**, *9*, 1902077.
[39] Q. Tian, M. Tang, F. Jiang, Y. Liu, J. Wu, R. Zou, Y. Sun, Z. Chen, R. Li, J. Hu, *Chem. Commun.* **2011**, *47*, 8100.
[40] X. Wang, L. Tian, X. Long, M. Yang, X. Song, W. Xie, D. Liu, Y. Fu, J. Li, Y. Li, D. He, *Sci. China Mater.* **2021**, *64*, 1632.
[41] X. Cai, X. Shen, L. Ma, Z. Ji, L. Kong, *RSC Adv.* **2015**, *5*, 58777.
[42] S. Li, J. Chen, J. Xiong, X. Gong, J. Ciou, P. S. Lee, *Nano-Micro Lett.* **2020**, *12*, 34.
[43] F. A. Stevie, C. L. Donley, *J. Vac. Sci. Technol., A* **2020**, *38*, 063204.
[44] M. C. Biesinger, B. P. Payne, L. W. M. Lau, A. Gerson, R. S. C. Smart, *Surf. Interface Anal.* **2009**, *41*, 324.
[45] L. Fu, Z. Liu, Y. Liu, B. Han, P. Hu, L. Cao, D. Zhu, *Adv. Mater.* **2005**, *17*, 217.
[46] A. M. Elshahawy, X. Li, H. Zhang, Y. Hu, K. H. Ho, C. Guan, J. Wang, *J. Mater. Chem. A* **2017**, *5*, 7494.

ADVANCED
SCIENCE NEWS

www.advancedsciencenews.com

NANO · MICRO

small

www.small-journal.com

[47] D. L. Legrand, H. W. Nesbitt, G. M. Bancroft, *Am. Mineral.* **1998**, *83*, 1256.

[48] L. Shen, J. Wang, G. Xu, H. Li, H. Dou, X. Zhang, *Adv. Energy Mater.* **2015**, *5*, 1400977.

[49] J. Cao, Y. Hu, Y. Zhu, H. Cao, M. Fan, C. Huang, K. Shu, M. He, H. C. Chen, *Chem. Eng. J.* **2021**, *405*, 126928.

[50] A. Molina, N. Patil, E. Ventosa, M. Liras, J. Palma, R. Marcilla, *Adv. Funct. Mater.* **2020**, *30*, 1908074.

[51] A. Molina, N. Patil, E. Ventosa, M. Liras, J. Palma, R. Marcilla, *ACS Energy Lett.* **2020**, *5*, 2945.

[52] B. Pierozynski, *Int. J. Electrochem. Sci.* **2011**, *6*, 860.

[53] W. S. Hummers, R. E. Offeman, *J. Am. Chem. Soc.* **1958**, *80*, 1339.

[54] J. Chen, B. Yao, C. Li, G. Shi, *Carbon* **2013**, *64*, 225.

[55] S. Park, J. An, J. R. Potts, A. Velamakanni, S. Murali, R. S. Ruoff, *Carbon* **2011**, *49*, 3019.

[56] Z. Xia, G. Maccaferri, C. Zanardi, M. Christian, L. Ortolani, V. Morandi, V. Bellani, A. Kovtun, S. Dell'Elce, A. Candini, A. Liscio, V. Palermo, *J. Phys. Chem. C* **2019**, *123*, 15122.

[57] C. C. Lalau, C. T. J. Low, *Batteries Supercaps* **2019**, *2*, 551.

[58] S. Saha, M. Johnson, F. Altayaran, Y. Wang, D. Wang, Q. Zhang, *Electrochem* **2020**, *1*, 286.

[59] A. Irshad, N. Munichandraiah, *ACS Appl. Mater. Interfaces* **2017**, *9*, 19746.

[60] J. Y. Lin, J. H. Liao, S. W. Chou, *Electrochim. Acta* **2011**, *56*, 8818.

2106403 (12 of 12)